DTU Library

Detection of Be dopant pairing in VLS grown GaAs nanowires with twinning superlattices

Mead, Christopher; Huang, Chunyi; Isik Goktas, Nebile; Fiordaliso, Elisabetta Maria; LaPierre, Ray R.; Lauhon, Lincoln J.

Link back to DTU Orbit

PAPER • OPEN ACCESS

Detection of Be dopant pairing in VLS grown GaAs nanowires with twinning superlattices

To cite this article: Christopher Mead *et al* 2023 *Nanotechnology* **34** 385701

View the article online for updates and enhancements.

Detection of Be dopant pairing in VLS grown GaAs nanowires with twinning superlattices

Christopher Mead[1] , Chunyi Huang[1], Nebile Isik Goktas[2],
Elisabetta Maria Fiordaliso[3], Ray R LaPierre[2] and Lincoln J Lauhon[1]

[1] Department of Materials Science and Engineering, Northwestern University, Evanston, IL, United States of America
[2] Department of Engineering Physics, McMaster University, Hamilton, Ontario L8S 4L7, Canada
[3] DTU Nanolab, Technical University of Denmark, DK-2800 Kongens Lyngby, Denmark

E-mail: lauhon@northwestern.edu

CrossMark

Abstract

Control over the distribution of dopants in nanowires is essential for regulating their electronic properties, but perturbations in nanowire microstructure may affect doping. Conversely, dopants may be used to control nanowire microstructure including the generation of twinning superlattices (TSLs)—periodic arrays of twin planes. Here the spatial distribution of Be dopants in a GaAs nanowire with a TSL is investigated using atom probe tomography. Homogeneous dopant distributions in both the radial and axial directions are observed, indicating a decoupling of the dopant distribution from the nanowire microstructure. Although the dopant distribution is microscopically homogenous, radial distribution function analysis discovered that 1% of the Be atoms occur in substitutional-interstitial pairs. The pairing confirms theoretical predictions based on the low defect formation energy. These findings indicate that using dopants to engineer microstructure does not necessarily imply that the dopant distribution is non-uniform.

Supplementary material for this article is available online

(Some figures may appear in colour only in the online journal)

1. Introduction

Semiconductor nanowires of controlled size, shape, and crystal structure exhibit unique properties that are not accessible by conventional bulk and thin film growth methods [1–3], and are therefore a promising platform for advances in computation [4, 5], communication [6, 7], and energy conversion [8], among other applications. The vapor–liquid–solid (VLS) growth process [9, 10], in which a liquid droplet promotes the transfer of vapor-phase precursors into the solid nanowire, enables precise control of the nanowire diameter by controlling the droplet size [11]. In compound semiconductors such as group III-As and III-Sb materials, variations in the III/V ratio enable further control of faceting and the growth of wurtzite phase material, in addition to the bulk-stable zincblende phase [1, 12]. The ability to selectively grow wurtzite and zincblende phases, which have equivalent compositions but distinct electronic band structures, creates the opportunity to realize novel homojunctions [13–15]. Optimization of devices based on single phases or junctions between phases requires deterministic control of altered atomic stacking sequences and suppression of random stacking fault formation, which degrades charge carrier mobilities and lifetimes.

The introduction of dopants during III–V nanowire growth modifies the interfacial energies in the VLS droplet and can be used to suppress stacking fault formation [16, 17] or selectively grow zincblende and wurtzite phases [18] by modifying nucleation of crystal planes perpendicular to the

growth direction [19]. Furthermore, careful tuning of growth conditions and doping enables the growth of twinning superlattices (TSLs) consisting of periodic arrays of stacking faults [18, 20–24]. TSLs have been explored for applications in thermoelectrics [21] and optoelectronics [22, 23], where they provide an additional degree of freedom in engineering electronic and phononic band structure. While clear correlations have been established between doping and changes in microstructure, the understanding of the dopant distribution in TSLs is rather limited. Because twinning modifies the surface faceting of nanowires, it is likely to impact the dopant distribution in nanowires for which surface accumulation [25, 26] and facet segregation [27, 28] have been observed. Indeed, scanning microwave impedance microscopy of GaAs nanowires with TSLs detected charge carrier accumulation coinciding with twin planes [24] suggesting the possibility of correlated segregation of dopants to twins or regions associated with twins. Such variations in doping produce substantial perturbations of the electronic properties and are in general undesirable. Hence, it is important to understand whether the deterministic growth of TSLs with a uniform dopant distribution is possible.

Here we report the distribution of Be dopants in VLS-grown GaAs nanowires with TSLs using atom probe tomography (APT). TSL nanowires have average Be concentrations of $\sim$1–2 $\times$ 10^{19} cm^{-3}, and the dopants are distributed homogeneously in both the radial and axial directions, indicating a decoupling of the dopant spatial distribution from the perturbations in microstructure. There is no evidence for periodic modulation of the dopant concentration, and no evidence of dopant segregation or clustering. Intriguingly, we find that $\sim$1% of Be atoms are found paired with another Be atom. The measured Be–Be radial distribution function (RDFs) is consistent with prior theoretical calculations [29] that predict formation of substitutional-interstitial pairs of Be dopants in GaAs. Our finding also agrees with a prior report of a defect complex including a Be interstitial in Be-doped GaAs nanowires characterized with Raman spectroscopy [30]. Due to their low abundance, the dopant pairs will not significantly impact the electronic properties of the nanowires.

2. Experimental methods

GaAs nanowires were grown on (111) Si substrates by molecular beam epitaxy using the selective-area, self-assisted, VLS process as described previously [20]. Selective-area epitaxy of the nanowires was achieved using a silicon oxide mask patterned by electron beam lithography into an array of holes with 360 nm pitch. Be doping was introduced in a self-catalyzed VLS growth process driven by a Ga droplet at the nanowire tip. The V/III flux ratio was decreased concomitantly with the onset of Be doping to increase the Ga droplet size during growth of the TSL region. The TSL was grown for a duration of 30 min by introducing Be dopant flux corresponding to a thin film carrier concentration of 10^{20} cm^{-3}. The nanowire growth temperature was 510 °C and

V/III flux ratio was 0.5. Scanning electron microscopy (SEM) was performed with an FEI 400 ACE, and transmission electron microscopy (TEM) was performed with a JEOL 2010F TEM with 200 kV.

APT samples were prepared by scraping a TEM grid across the growth substrate to mount nanowires on the grid as shown in figure S1. The nanowires are then individually mounted on tungsten wires with the TSL end of the nanowire pointing away from the wire. FIB milling was performed using an FEI Helios dual-beam focused ion-beam (FIB) microscope to sharpen the top of the nanowires into tips with diameters $\sim$50 nm which are required to run in APT. To maintain uniform radial milling, the samples were tilted 7 degrees off axis of the ion beam and milled in 60 degree rotational increments with each facet of the wire being exposed equally to the beam. Final cleaning and sharpening of the tips were performed head on to the ion beam and at lower energies to remove any regions of Ga implantation and avoid any further implantation into the samples.

APT was done using a local-electrode atom-probe (LEAP) 5000 XS (Cameca, Madison, WI). The samples were run at a temperature of 30 K and a background pressure of 5 $\times$ 10^{-11} Torr. A 355 nm ultraviolet laser was used to evaporate the sample at a pulse rate of 250 kHz and pulse energy of 0.8 pJ.

IVAS 3.8.6 was used to reconstruct the APT data and provide the atomic spatial distribution information. Spacing between Ga atoms corresponding to (111) planes was observed in the center of the reconstructions and the image compression factor of the reconstructions were adjusted so that this spacing corresponded with the theoretical spacing between (111) planes.

3. Results and discussion

A representative SEM image of the nanowires on the substrate is shown in figure 1(a). Figure 1(b) shows a representative TEM image of a nanowire after removal from the growth substrate and mounting on a copper grid. The small perturbations of the nanowire facets visible in figure 1(a) are associated with the twinning observed in figure 1(b), indicating that the zincblende twins occur at a regular interval of 20–25 nm.

An APT analysis run in which 23.8 million ions were collected resulted in the mass spectrum and sample reconstruction in figures 1(c) and (d), respectively. Be$^+$ and Be^{2+} peaks are observed at 9.0 Da and 4.5 Da, respectively as shown in figure 1(c), inset. The average Be concentration in the reconstructed volume is 1.5 $\times$ 10^{19} cm^{-3}, which is consistent with concentration measurements of 1.7 $\times$ 10^{19} cm^{-3} and 1.8 $\times$ 10^{19} cm^{-3} in two additional nanowires analyzed by APT. The measured Be concentration is lower than the dopant concentration of 10^{20} cm^{-3} that would result if all atoms in the Be and Ga fluxes were directly incorporated into the nanowire. This difference may indicate a saturation of Be dopant incorporation as was previously observed in self-catalyzed GaAs nanowires [17]. The majority of other ions
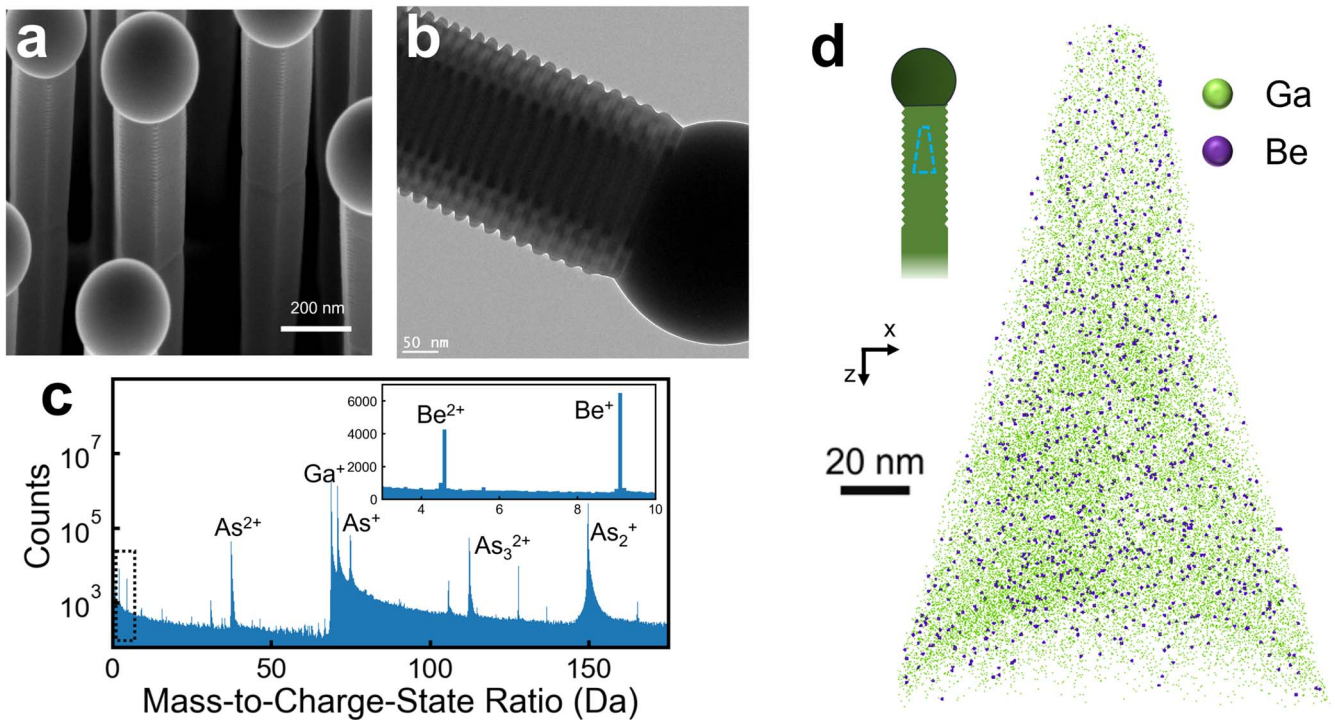
Figure 1. (a) SEM image of Be-doped GaAs nanowires, showing perturbations to the sidewall facets below the Ga droplet. (b) TEM image near the top of the nanowire showing the TSL. (c) The mass spectrum of the sample evaporated in APT showing major peaks related to Ga and As ions in addition to the Be dopant peaks (inset). (d) The corresponding reconstruction of the evaporated sample with a fraction of Be and Ga ions displayed. The blue trapezoid in the inset schematic shows the location of the region analyzed in APT relative to the nanowire structure.

detected in the APT measurement are attributable to atomic and molecular ions of either Ga or As. Because the fraction of As ions detected in pulsed-laser APT varies sensitively with analysis conditions [31], the Be concentration in a given volume is calculated as the number of Be atoms divided by twice the number of Ga atoms assuming equivalent detection efficiencies for Be and Ga. This is a reasonable assumption because evaporation of both species is dominated by single ions without evidence of correlated evaporation. The three-dimensional reconstruction of the analyzed region shown in figure 1(d) was generated using commercial software (IVAS 3.8.6, Cameca, Madison, WI). Be atoms are observed throughout the reconstructed volume with no obvious variations in concentration. The tapered shape of the reconstruction reflects the shape of the sharpened sample after FIB processing (blue trapezoid in figure 1(d) schematic), rather than the shape of the as-grown nanowire. The approximate location of the reconstructed region, centered on the TSL region of interest, is illustrated in the inset schematics.

To quantitatively analyze variations in Be concentration that might reveal correlations with the TSL, one-dimensional composition profiles along the growth axis were extracted as shown in figure 2(a). The Be concentration, averaged across the nanowire diameter, decreases from $\sim 2.0 \times 10^{19}$ to $\sim 1.3 \times 10^{19}$ cm^{-3} over a distance of 170 nm. To isolate any rapid variations in Be concentration, the slow variation in average composition was fit empirically with a quadratic polynomial function, which was subtracted from the original data. Figure 2(b) shows the resulting variations plotted in

terms of the local change in composition, with points in blue and red showing differences exceeding one standard variation. No periodic variations in the Be concentration are observed on the length scale of the twin spacing (20–25 nm). Hence, we conclude that Be can be used to induce TSL formation without creating associated variations in dopant density that would introduce unwanted variations in carrier concentration and electric fields.

Because radial variations in dopant concentration have been reported in nanowires grown by a VLS process [28, 32], figure 2(c) plots the Be concentration perpendicular to the growth direction. The concentration values at each position represent an average over the depth of entirety of the reconstruction. The diameter shown in figure 2(c) is smaller than the diameter of the reconstruction in figure 1(d) to exclude regions with insufficient counts to report reliable dopant concentrations. We observe no systematic variations in Be concentration across the reconstruction, though as a caveat, the reconstruction does not include the surface of the nanowire, which was milled during sample preparation to create a sufficiently sharp tip. The magnitude of the fluctuations are comparable to those observed in figure 2(b) and are attributed to counting statistics.

The analysis above demonstrates that the dopant concentration is homogeneous on the length scale of a few to tens of nanometers, and that observed fluctuations are consistent with a random dopant distribution. Provided that the Be is incorporated substitutionally on Ga sites, the carrier concentration will also be uniform. However, given the relatively
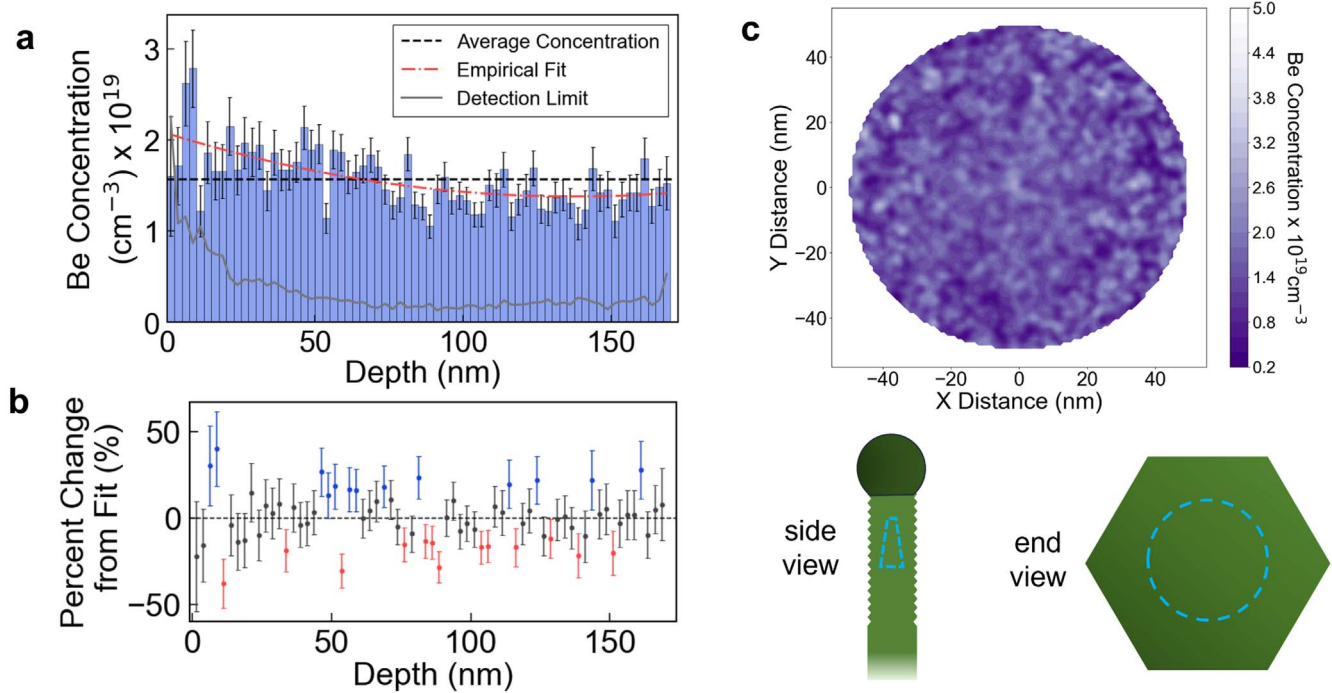
Figure 2. (a) The Be concentration in the TSL region as a function of depth, moving towards the bottom of the nanowire. The detection limit is given by the gray line. The dashed red line shows an empirical fit that captures gradual variations in the average concentration. (b) Local variations in Be concentration relative to the empirical fit shown in (a). Blue and red points represent fluctuations greater than one standard deviation from the average background. (c) Two-dimensional plot of the radial Be concentration averaged over the depth of the reconstruction (∼170 nm). The lower limit of the color bar is the Be detection limit. The schematics show the approximate location of the region captured in APT analysis.

high dopant concentration used to induce the perturbations in twinning, it is important to consider the finite solubility of Be in Ga and whether the dopants are in fact incorporated on active sites. Spectroscopic signatures of Be dopant pairing have been reported for both Si [33] and GaAs [30]. Furthermore, first principles calculations predict that the formation of pairs of Be atoms in substitutional and interstitial sites (Be_i–Be_{Ga}) with a net positive charge is energetically favorable in GaAs [29]. Although APT does not generally achieve the necessary spatial resolution to distinguish between substitutional and interstitial sites, it is feasible to analyze the atomic scale distribution of Be atoms to look for evidence of excess pairing that is theoretically predicted.

Towards this end, the Be–Be RDFs was generated and plotted in figure 3. The RDF plots the relative likelihood of encountering a Be atom at a given radial distance given the presence of a Be atom at zero nm; a value of 1 represents the likelihood relative to the average concentration of the matrix. Normalized RDFs are generated using the formula $RDF = \frac{1}{C_i^0}\sum_{k=1}^{N_j} \frac{N_i^k(r)}{N_{tot}^k(r)}$ where j is the species with which the distance to atoms of species i is determined. The quantity of species i within a particular radius of species j is divided by the total number of all species within that radius and normalized by the average concentration of species i throughout the sample. Deviations from unity indicate deviations from a random distribution of atoms. The RDF was generated using ions within a 15 nm radius of the center of the reconstruction because the region near the (111) crystallographic pole
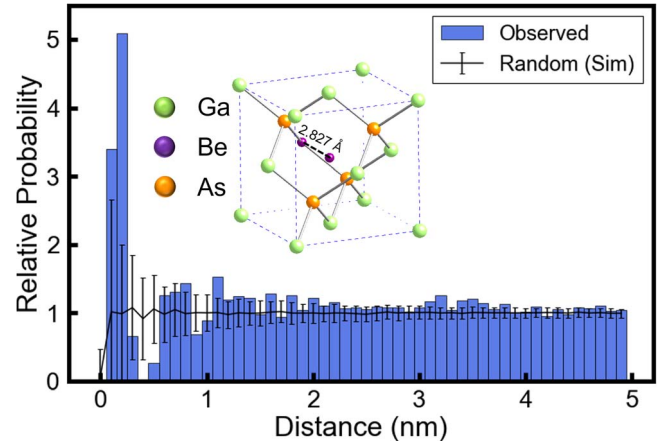
Figure 3. The Be–Be RDF for the 15 nm radial region in the center of the reconstruction. A floor function is applied to the values in the RDF so that each bar includes 0.1 nm worth of data. The black line is the mean value of the simulations of random Be substitution-only RDFs. The error bars encapsulate one standard deviation worth of the simulation data. The inset is a schematic of the GaAs unit cell with the structure of the Be_i–Be_{Ga} pair with the distance between the substitutional and interstitial sites shown.

exhibits a higher local order than the outer portions of the reconstruction, as shown in figure S2; such poles have been found to maintain more pairing information in RDFs [34]. A significant excess in Be is observed at a distance of 0.23 nm, i.e. there are many more pairs of Be atoms ∼0.23 nm apart than would be expected in a random distribution. A similar

excess at ∼0.2 nm was observed in two additional APT reconstructions shown in figure S3. Furthermore, there is an associated deficit at ∼0.4 nm, as expected if nearby Be atoms experience attractive interactions that drive pairing. We note that, given the average Be spacing of 4.1 nm, reconstruction of the surface lattice would not induce sufficient changes in atomic positions to produce the observed peak. The frequency distribution analysis shown in table S1 also shows an excess of voxels containing two Be atoms. We attribute the observed excess to the presence of pairs of Be atoms, such as interstitial-substitutional pairs (Be$_i$–Be$_{Ga}$), that have a low formation energy [29]. While the resolution of the RDF is, by inspection, sufficient to resolve the excess and deficit at ∼0.23 and ∼0.4 nm, respectively, the *accuracy* of the peak position is not sufficient to distinguish between distinct defect complexes involving substitutional and interstitial Be.

To confirm the statistical significance of the RDF peak, we compare the observed RDF with a simulated RDF, represented by the black line and data points in figure 3. The simulated RDF was generated by taking the distribution of Ga atoms in the APT reconstruction and randomly substituting Be atoms to achieve the measured average concentration. We use the Ga atom positions from the APT reconstruction, rather than a perfect lattice, to ensure that any non-ideal variations in local density are represented in the control distribution. For each random configuration of Be substituted on Ga sites, an RDF was calculated, and the process was repeated 180 times to obtain the average RDF and standard deviation for each bin in the distribution. The observed Be excess and deficit significantly exceed the standard deviation of the random distribution. For context, we note that the pairing of 1% of the Be dopants is sufficient to produce the observed excess. The impact on carrier concentration is therefore negligible since the majority of Be are likely to be on isolated substitutional sites. Given that migration of Be interstitials is believed to be responsible for the high diffusivity of Be in GaAs [35, 36], the observed uniformity of doping on the nanometer to tens of nanometer scale is perhaps not surprising.

4. Conclusion

In summary, the distribution of Be dopants in GaAs nanowires within regions of TSLs was analyzed by APT. Small variations in dopant concentration were observed along the growth direction, and the doping in the center of the nanowires was radially uniform. There are no correlations between dopant concentration and twins, indicating that Be doping can be used to create microstructure without creating perturbations in carrier concentration or electric field. A predicted pairing of Be atoms was observed that is attributed to the low formation energy of substitutional-interstitial pairs. Be–Be pairing in GaAs has not been previously observed, nor has dopant pairing been previously reported in nanowire materials.

Data availability statement

The data that support the findings of this study will be openly available following an embargo at the following URL/DOI: https://doi.org/10.18126/QT7U-G58D. Data will be available from 14 September 2023.

ORCID iDs

Christopher Mead ⓘ https://orcid.org/0009-0008-5071-9327
Ray R LaPierre ⓘ https://orcid.org/0000-0003-4598-8940
Lincoln J Lauhon ⓘ https://orcid.org/0000-0001-6046-3304

References

[1] Yuan X *et al* 2021 Selective area epitaxy of III–V nanostructure arrays and networks: growth, applications, and future directions *Appl. Phys. Rev.* **8** 021302
[2] Zhang Y, Wu J, Aagesen M and Liu H 2015 III–V nanowires and nanowire optoelectronic devices *J. Phys. Appl. Phys.* **48** 463001
[3] Barrigón E, Heurlin M, Bi Z, Monemar B and Samuelson L 2019 Synthesis and applications of III–V nanowires *Chem. Rev.* **119** 9170–220
[4] Mourik V *et al* 2012 Signatures of Majorana fermions in hybrid superconductor-semiconductor nanowire devices *Science* **336** 1003–7

[5] Zhang H, Liu D E, Wimmer M and Kouwenhoven L P 2019 Next steps of quantum transport in Majorana nanowire devices *Nat. Commun.* **10** 5128

[6] Mårtensson T *et al* 2004 Epitaxial III−V nanowires on silicon *Nano Lett.* **4** 1987–90

[7] Quan L N, Kang J, Ning C-Z and Yang P 2019 Nanowires for photonics *Chem. Rev.* **119** 9153–69

[8] Goktas N I *et al* 2018 Nanowires for energy: a review *Appl. Phys. Rev.* **5** 041305

[9] Ek M and Filler M A 2018 Atomic-scale choreography of vapor–liquid–solid nanowire growth *Acc. Chem. Res.* **51** 118–26

[10] Wagner A R and Ellis S W 1964 Vapor–liquid–solid mechanism of single crystal growth *Appl. Phys. Lett.* **4** 89–90

[11] Kim W *et al* 2018 Bistability of contact angle and its role in achieving quantum-thin self-assisted GaAs nanowires *Nano Lett.* **18** 49–57

[12] Joyce H J, Wong-Leung J, Gao Q, Tan H H and Jagadish C 2010 Phase perfection in zinc blende and Wurtzite III−V nanowires using basic growth parameters *Nano Lett.* **10** 908–15

[13] Rieger T, Lepsa M I, Schäpers T and Grützmacher D 2013 Controlled wurtzite inclusions in self-catalyzed zinc blende III–V semiconductor nanowires *J. Cryst. Growth* **378** 506–10

[14] Lähnemann J *et al* 2019 Correlated nanoscale analysis of the emission from Wurtzite versus Zincblende (In,Ga)As/GaAs nanowire core–shell quantum wells *Nano Lett.* **19** 4448–57

[15] Dubrovskii V G, Sibirev N V, Halder N N and Ritter D 2019 Classification of the morphologies and related crystal phases of III–V nanowires based on the surface energy analysis *J. Phys. Chem.* C **123** 18693–701

[16] Ajay A *et al* 2022 Enhanced growth and properties of non-catalytic GaAs nanowires via Sb surfactant effects *Appl. Phys. Lett.* **121** 072107

[17] Zhang Y *et al* 2018 Doping of self-catalyzed nanowires under the influence of droplets *Nano Lett.* **18** 81–7

[18] Algra R E *et al* 2008 Twinning superlattices in indium phosphide nanowires *Nature* **456** 369–72

[19] Zhang Z *et al* 2018 *In situ* TEM observation of crystal structure transformation in InAs nanowires on atomic scale *Nano Lett.* **18** 6597–603

[20] Isik Goktas N, Sokolovskii A, Dubrovskii V G and LaPierre R R 2020 Formation mechanism of twinning superlattices in doped GaAs nanowires *Nano Lett.* **20** 3344–51

[21] Ghukasyan A and LaPierre R 2022 Thermal transport in twinning superlattice and mixed-phase GaAs nanowires *Nanoscale* **14** 6480–7

[22] Xue M *et al* 2020 Observation and ultrafast dynamics of inter-sub-band transition in InAs twinning superlattice nanowires *Adv. Mater.* **32** 2004120

[23] Qian Y, Xu K, Cheng L, Li C and Wang X 2021 Rapid, facile synthesis of InSb twinning superlattice nanowires with a high-frequency photoconductivity response *RSC Adv.* **11** 19426–32

[24] Choi W *et al* 2017 Direct electrical probing of periodic modulation of zinc-dopant distributions in planar gallium arsenide nanowires *ACS Nano* **11** 1530–9

[25] Czaban J A, Thompson D A and LaPierre R R 2009 GaAs core–shell nanowires for photovoltaic applications *Nano Lett.* **9** 148–54

[26] Fukata N *et al* 2011 Segregation behaviors and radial distribution of dopant atoms in silicon nanowires *Nano Lett.* **11** 651–6

[27] Friedl M *et al* 2018 Template-assisted scalable nanowire networks *Nano Lett.* **18** 2666–71

[28] Dastjerdi M H T *et al* 2017 Three-fold symmetric doping mechanism in GaAs nanowires *Nano Lett.* **17** 5875–82

[29] Kulish V, Liu W, Benistant F and Manzhos S 2018 Dopant–dopant interactions in beryllium doped indium gallium arsenide: an *ab initio* study *J. Mater. Res.* **33** 401–13

[30] Hilse M, Ramsteiner M, Breuer S, Geelhaar L and Riechert H 2010 Incorporation of the dopants Si and Be into GaAs nanowires *Appl. Phys. Lett.* **96** 193104

[31] Gorman B P, Norman A G and Yan Y 2007 Atom probe analysis of III–V and Si-based semiconductor photovoltaic structures *Microsc. Microanal.* **13** 493–502

[32] Salehzadeh O, Kavanagh K L and Watkins S P 2012 Controlled axial and radial Te-doping of GaAs nanowires *J. Appl. Phys.* **112** 054324

[33] Killoran N, Dunstan D J, Henry M O, Lightowlers E C and Cavenett B C 1982 The isoelectronic centre in beryllium-doped silicon. I. Zeeman study *J. Phys. C: Solid State Phys.* **15** 6067

[34] Haley D, Petersen T, Barton G and Ringer S P 2009 Influence of field evaporation on radial distribution functions in atom probe tomography *Phil. Mag.* **89** 925–43

[35] Deal M D and Robinson H G 1989 Diffusion of implanted beryllium in n- and p-type GaAs *Appl. Phys. Lett.* **55** 1990–2

[36] Yu S, Tan T Y and Gösele U 1991 Diffusion mechanism of zinc and beryllium in gallium arsenide *J. Appl. Phys.* **69** 3547–65